Received: 15 November 2021 | Revised: 3 April 2022 | Accepted: 2 May 2022 | Published on: 4 July 2022

DOI: 10.1002/qj.4324

Quarterly Journal of the Royal Meteorological Society RMetS

RESEARCH ARTICLE

Formation of maritime convergence zones within cold air outbreaks due to the shape of the coastline or sea ice edge

Shun-ichi I. Watanabe[1] | **Hiroshi Niino**[2] | **Thomas Spengler**[3,4]

[1]Meteorological Research Institute, Tsukuba, Japan

[2]Atmosphere and Ocean Research Institute, The University of Tokyo, Tokyo, Japan

[3]Geophysical Institute, University of Bergen, Bergen, Norway

[4]Bjerknes Centre for Climate Research, Bergen, Norway

Correspondence
Shun-ichi I. Watanabe, Department of Physical Meteorology Research, Meteorological Research Institute, Tsukuba, Ibaraki, 305-0052, Japan.
Email: swatanabe@mri-jma.go.jp

Funding information
Japan Society for the Promotion of Science, Grant/Award Numbers: 17K14390, 21H01164, 19K03967; MEXT Program for Promoting Researches on the Supercomputer Fugaku (Large Ensemble Atmospheric and Environmental Prediction for Disaster Prevention and Mitigation); Research Council of Norway project NORPAN, Grant/Award Number: 250135

Abstract

Maritime cold air outbreaks often feature convergence zones that provide a conducive environment for the development of polar mesoscale cyclones and polar lows. This study examines the formation mechanisms of these convergence zones in cold air outbreaks downstream of a coastline or sea-ice edge. A simplified configuration in which the coastline or sea-ice edge is approximated by a line featuring a bend with an angle is examined using analytic solutions and idealised numerical simulations. The bend of the coastline causes differences in the fetch over which air parcels travel, causing a warm wedge of air downstream of the bend due to differential airmass transformations. The warm wedge is associated with a pressure trough that leads to convergence in the presence of surface friction. The analytic model captures this mechanism and compares well with the idealised numerical simulations. Condensational heating associated with moist convection enhances vertical motions and thus intensifies the horizontal convergence. The idealised numerical simulations also reproduce an asymmetry in the vertical shear of the horizontal wind across the convergence zone, which explains the transverse cloud streets downstream to the left of the convergence zone.

KEYWORDS

cold air outbreak, convergence zone, analytic model, idealised numerical simulation

1 | INTRODUCTION

When cold air originating over land or sea ice is advected over relatively warmer water during so-called marine cold air outbreaks (CAOs), a large amount of surface sensible and latent heat fluxes is provided to the atmosphere (e.g., Burke, 1945; Asai, 1965; Papritz and Spengler, 2017; Terpstra *et al.*, 2021). These CAOs regularly promote convergence zones that are often accompanied by a cloud band, where the morphology of the cloud band depends on both the shape of the water body and the wind direction (Laird *et al.*, 2003), with the optimal wind direction being parallel to the long axis of the water body (Norris *et al.*, 2013). These convergence zones commonly feature horizontal shear and baroclinicity, thereby providing a conducive environment for significant weather, such as polar lows and other polar mesocyclones (Watanabe and Niino, 2014; Sergeev *et al.*, 2017; Spengler *et al.*, 2017; Watanabe *et al.*, 2018; Terpstra and Watanabe, 2020; Stoll *et al.*, 2021). To better understand the effects of the shape

of a coastline or sea-ice edge on the formation and intensity of these convergence zones, in this study we assess and quantify their impact in isolation.

Typical examples of such convergence zones and cloud bands are found over the Great Lakes (e.g., Laird *et al.*, 2017), the English Channel (Norris *et al.*, 2013), the Irish Sea (Norris *et al.*, 2013), the Gulf of Finland (Mazon *et al.*, 2015; Savijärvi, 2015), and the Baltic Sea (Andersson and Gustafsson, 1994). They can also extend far downstream over an open water, such as the cloud band associated with the Japan Sea Polar Airmass Convergence Zone (JPCZ; Asai, 1988) that regularly develops with its origin in the northwestern corner of the Japan Sea extending southeastward (Figure 1a). The JPCZ often spins up polar lows and polar mesocyclones (e.g., Watanabe *et al.*, 2016; Yanase *et al.*, 2016). Similar cloud bands are also observed over the Atlantic Ocean (Atlas *et al.*, 1983) and the Nordic Seas (Figure 1b; Sergeev *et al.*, 2018, where polar lows form regularly (e.g., Terpstra *et al.*, 2016; Michel *et al.*, 2018).

Combined effects—such as the convergence of land breezes caused by the thermal contrast between land and water, and the frictional difference between land and water surfaces—have generally been considered to be responsible for the formation of low-level convergence zones (Laird *et al.*, 2003; Savijärvi, 2012; Steenburgh and Campbell, 2017). However, these processes cannot play a significant role for convergence zones that occur far downstream of a coastline or sea-ice edge over the open ocean. Coupled aspects with the ocean can also play a significant role in shaping surface fluxes and impact on the ocean (e.g., Renfrew *et al.*, 2019).

Numerical studies suggest that the thermal contrast between the Korean Peninsula and the Japan Sea, a large sea-surface temperature (SST) gradient, and topography contribute to the formation of the JPCZ (Nagata *et al.*, 1986; Nagata, 1991; Shinoda *et al.*, 2021). In addition, the underlying SST distribution can also affect the structure of the convergence zone due to variations in the surface fluxes, as well as a difference in fetch due to the geometry of the coastline or sea-ice edge that can lead to different exposures to surface sensible and latent heat fluxes (Atlas *et al.*, 1983). Even though orography has recently been argued to be a major cause of the JPCZ (Shinoda *et al.*, 2021), we still lack a fundamental understanding for the formation of convergence zones in different coastal set-ups without the additional complexity of topography. Model resolution and sea-ice distribution in the marginal ice can also play a dominant role in shaping the simulated variations of surface fluxes with a fetch (Spensberger and Spengler, 2021). To gain a more detailed understanding, it is best to isolate different mechanisms and their impact on the asymmetry in the airmass transformation. We investigate the effect of a difference in the fetch for the formation of a convergence zone, where the shape of a coastline or sea-ice edge is a primary factor determining a difference in the fetch. Although topography can also cause an asymmetry in the fetch (West and Steenburgh, 2022), we will focus on the role of the shape of a coastline or sea-ice edge in the formation of a convergence zone to isolate this effect. Other factors, such as topography, are of interest for future work.

In addition to the main cloud band of the convergence zone, a convectively mixed layer accompanied with cellular convection or horizontal convective rolls forms, depending on the wind profile and the static stability of the atmosphere (e.g., Atkinson and Zhang, 1996). For example, transverse cloud streets to the northeast of the JPCZ are normal to the JPCZ cloud band, whereas longitudinal cloud streets to the southeast are parallel to it (Murakami, 2019; Steenburgh and Nakai, 2020) (Figure 1a). Cloud streets parallel and perpendicular to the main cloud band are also found to the north and south, respectively, of the upper left cloud band in Figure 1b. This difference in the direction of the cloud streets has been argued to be caused by roll convection parallel to the axis of the vertical wind shear vector (Eito *et al.*, 2010). The direction of vertical shear is different between the northeast and southwest sides of the JPCZ (Nagata, 1987), and it is parallel to the direction of the cloud streets, in accordance with linear theory (Asai, 1972). What causes the difference in the direction of the vertical wind shear vector, however, is not fully understood.

To assess and quantify the effects of the shape of the coastline or sea-ice edge on airmass transformation and formation of the convergence zone, we consider a simplified configuration of the shape of the coastline. To gain a deeper physical understanding, we derive an analytic solution for a simplified model (see Section 2) and perform idealised numerical simulations (see Section 3), where we vary the simplified shape of the coastline allowing for variations in the fetch within the CAO. The analytic solution is compared with the numerical simulations and used to interpret the numerical results.

2 | ANALYTIC MODEL

To investigate the influence of a bend in the coastline or sea-ice edge, we consider a simple analytic model with a dry Boussinesq atmosphere. The conditions resemble a marine CAO with a coastline or sea-ice edge represented by two straight lines meeting at an angle of ϕ at y_c = 1,000 km on an f-plane (Figure 2).

The atmosphere over land or sea ice is assumed to be stratified with a constant lapse rate Γ, yielding the basic state potential temperature

$$\overline{\theta} = \theta_s + \Gamma z, \tag{1}$$

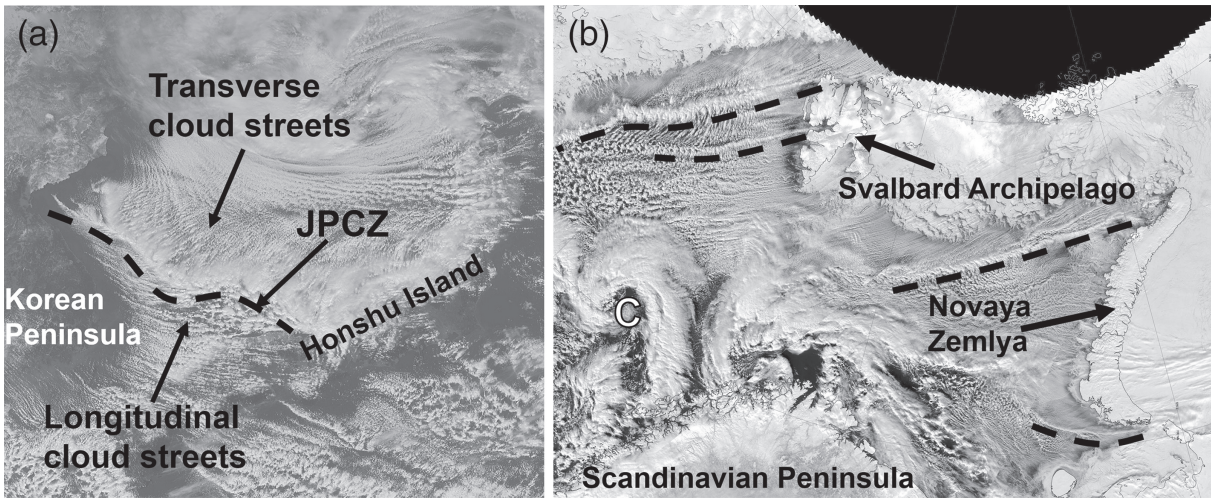

FIGURE 1 (a) Satellite image from Himawari-8 visible band at 0300 UTC on January 24, 2018. Note that longitudinal and transverse clouds exist to the southwest and northeast, respectively, of the Japan Sea Polar Airmass Convergence Zone (JPCZ). (b) NASA Worldview satellite image of the Barents and Nordic Seas featuring several convergence zones and mesoscyclones on March 6, 2013. The Svalbard Archipelago, Novaya Zemlya, and the northern Norwegian coast are visible. The dashed lines indicate convergence cloud bands, and "C" in (b) indicates a mesoscale cyclone [Colour figure can be viewed at wileyonlinelibrary.com]

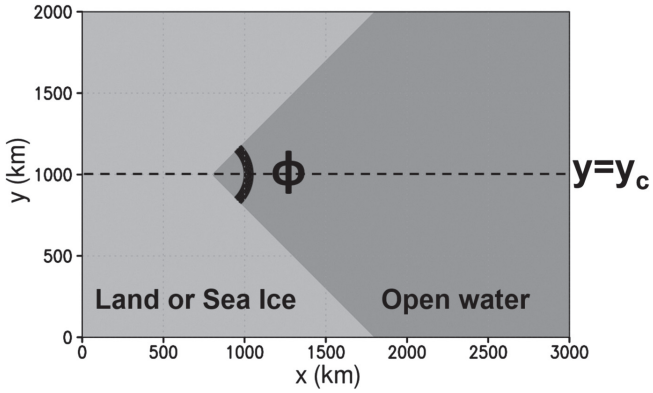

FIGURE 2 Schematic of the model set-up, with the green area (left side of the figure) representing land or sea ice and the blue area (right side of the figure) indicating open water [Colour figure can be viewed at wileyonlinelibrary.com]

where θ_s is the basic state potential temperature at the surface. We assume that the CAO features a uniform basic state zonal flow $\overline{u}$ without vertical shear and that the basic state is in hydrostatic balance

$$\frac{d\overline{p}}{dz} = -\rho_0 g \tag{2}$$

and geostrophic balance

$$f\overline{u} = -\frac{1}{\rho_0}\frac{d\overline{p}}{dy}, \tag{3}$$

where $\overline{p}$ is pressure, ρ_0 is basic state density, and g is gravitational acceleration.

The thermodynamic equation including vertical mixing is

$$\frac{D\theta}{Dt} = -\frac{\partial}{\partial z}(\overline{w'\theta'}), \tag{4}$$

where $\overline{w'\theta'}$ is the turbulent heat flux. Assuming a steady state with uniform flow $\overline{u}$, Equation (4) becomes

$$\overline{u}\frac{\partial\theta}{\partial x} = -\frac{\partial}{\partial z}(\overline{w'\theta'}). \tag{5}$$

Integrating Equation (5) from the surface ($z = 0$) to the top of the mixed layer ($z = h$) yields the convective mixed-layer equation:

$$\overline{u}\int_0^h \frac{\partial\theta}{\partial x}\,dz = \overline{u}h\frac{\partial\theta_A}{\partial x} = -\int_0^h \frac{\partial}{\partial z}(\overline{w'\theta'})\,dz = -\left[\overline{w'\theta'}\right]_{z=0}^{z=h}, \tag{6}$$

where h and θ_A are the height and potential temperature of the mixed layer, respectively. Neglecting entrainment at the top of the mixed layer (i.e., $\overline{w'\theta'}|_{z=0} = 0$), Equation (6) becomes

$$\overline{u}h\frac{\partial\theta_A}{\partial x} = F, \tag{7}$$

where F is the surface sensible heat flux (i.e., $\overline{w'\theta'}|_{z=0} = F$). Using the bulk formula, we obtain

$$F = c_H\overline{u}(\theta_{SST} - \theta_A), \tag{8}$$

where c_H is the heat exchange coefficient and θ_{SST} is the sea-surface potential temperature.

As the height of the mixed layer satisfies

$$h = \frac{\theta_A - \theta_s}{\Gamma}, \tag{9}$$

the equation for θ_A becomes

$$\frac{\partial \theta_A}{\partial x} = c_H \Gamma \frac{\theta_{SST} - \theta_A}{\theta_A - \theta_s}. \tag{10}$$

The pressure perturbation p' is associated with the potential temperature perturbation θ' through hydrostatic balance

$$\frac{dp'}{dz} = g\rho_0 \frac{\theta'}{\theta_0}, \tag{11}$$

where

$$\theta' = \theta_A - \overline{\theta} = \theta_A - (\theta_s + \Gamma z). \tag{12}$$

Integrating Equation (11) vertically from the surface to the top of the mixed layer and assuming $p' = 0$ at the top of the mixed layer yields

$$-p'_s = \rho_0 \frac{g}{\theta_0} \int_0^h \theta' \, dz = \rho_0 \frac{g}{\theta_0} \frac{(\theta_A - \theta_s)^2}{2\Gamma}, \tag{13}$$

where p'_s is the surface pressure perturbation. Differentiating Equation (13) with respect to x and using Equation (10) yields

$$\frac{\partial p'_s}{\partial x} = -\rho_0 \frac{g}{\theta_0} \frac{(\theta_A - \theta_s)}{\Gamma} \frac{\partial \theta_A}{\partial x} = -\rho_0 \frac{g c_H}{\theta_0} (\theta_{SST} - \theta_A). \tag{14}$$

If the meridional wind perturbation is much smaller than the basic state zonal wind, the fetch D (i.e., the length of the air parcel trajectory over open water) may be written as $D(x, y) = x - x_0(y)$, where $x_0(y)$ is the location of the coastline or sea-ice edge. As $\theta_A = \theta_s$ and $p_s = 0$ at $x = x_0(y)$, Equations (10) and (14) can be written as

$$\frac{d\theta_A}{dD} = c_H \Gamma \frac{\theta_{SST} - \theta_A}{\theta_A - \theta_s} \tag{15}$$

and

$$\frac{dp'_s}{dD} = -\rho_0 \frac{g c_H}{\theta_0} (\theta_{SST} - \theta_A). \tag{16}$$

We can calculate the surface wind components induced by this pressure perturbation by assuming a balance between the pressure gradient force, the Coriolis force, and friction:

$$-fv' = -\frac{1}{\rho_0} \frac{\partial p'_s}{\partial x} - \nu u' \tag{17}$$

and

$$fu' = -\frac{1}{\rho_0} \frac{\partial p'_s}{\partial y} - \nu v', \tag{18}$$

where friction is assumed to be proportional to the velocity with the friction coefficient ν. Solving for the perturbation wind components, Equations (17) and (18) yield

$$u' = -\frac{1}{\rho_0(\nu^2 + f^2)} \left(\nu \frac{\partial p'_s}{\partial x} + f \frac{\partial p'_s}{\partial y} \right) \tag{19}$$

and

$$v' = \frac{1}{\rho_0(\nu^2 + f^2)} \left(f \frac{\partial p'_s}{\partial x} - \nu \frac{\partial p'_s}{\partial y} \right), \tag{20}$$

where the perturbation pressure gradient components for the coastline or sea-ice edge in Figure 2 can be expressed as

$$\frac{\partial p'_s}{\partial x} = \frac{dp'_s}{dD} \frac{\partial D}{\partial x} = \frac{dp'_s}{dD} \tag{21}$$

and

$$\frac{\partial p'_s}{\partial y} = \frac{dp'_s}{dD} \frac{\partial D}{\partial y} = \begin{cases} -\frac{dp'_s}{dD} \tan\frac{\phi}{2} & (y > y_c) \\ +\frac{dp'_s}{dD} \tan\frac{\phi}{2} & (y < y_c) \end{cases}. \tag{22}$$

Thus, the meridional perturbation pressure gradient has a discontinuity at $y = y_c$, resulting in velocity jumps:

$$\Delta u' = \frac{2f}{\rho_0(\nu^2 + f^2)} \frac{dp'_s}{dD} \tan\frac{\phi}{2} \tag{23}$$

and

$$\Delta v' = \frac{2\nu}{\rho_0(\nu^2 + f^2)} \frac{dp'_s}{dD} \tan\frac{\phi}{2}. \tag{24}$$

Equations (23) and (24) indicate the presence of either a horizontal shear zone when the Coriolis force is dominant or a convergence line when friction is dominant. Given the strong turbulent momentum transport associated with the high surface sensible heat fluxes in CAOs, friction usually dominates and a convergence zone forms along the centreline extension of the bend.

3 | SET-UP OF NUMERICAL SIMULATIONS

3.1 | Model

We use the Japan Meteorological Agency non-hydrostatic numerical model (Saito *et al.*, 2006) for our simulations, performing both dry and moist experiments, where the dry experiments do not include any water vapour. In both sets of experiments, the Mellor–Yamada–Nakanishi–Niino Level-3 boundary-layer parametrisation scheme (Nakanishi and Niino, 2006) and a bulk parametrisation scheme for surface fluxes (Beljaars and Holtslag, 1991) are

used. In the moist experiments, we use the Kain–Fritsch convection parametrisation scheme (Kain and Fritsch, 1990; Kain, 2004) and an explicit three-ice bulk microphysical scheme (Ikawa *et al.*, 1991) that predicts mixing ratios of water vapour, cloud water, rain, cloud ice, snow, graupel, and density of cloud ice. Radiation processes are not considered in our simulations. The surface roughness length over land is fixed, and that over sea is based on Beljaars (1995). This model configuration is similar to the previous operational regional forecast system used by the Japan Meteorological Agency (Japan Meteorological Agency, 2013), which had been validated against observations and had been shown to give the best performance.

3.2 | Experimental design

We use an f-plane set-up at 40° N, which is the typical latitude for the Japan Sea. We have also carried out experiments on an f-plane at 60° N, representing the geographic location of the Nordic Seas or the latitude around Antarctica (see Appendix). The model domain is 3,000 × 2,000 km^2 in the zonal (x) and meridional (y) direction, respectively, with a horizontal grid spacing of 5 km, where the origin $(x, y) = (0, 0)$ is located in the southwestern corner of the model domain. There are 80 levels in the vertical, where the level spacing changes from about 20 m at the lowest levels to about 400 m at the top of the domain at 16.6 km. The boundary conditions are open in the zonal direction, whereas rigid free-slip boundaries are employed at the meridional and vertical boundaries with Rayleigh damping applied near the top of the model domain. The lower surface of the domain consists of sea and land, which features a bent coastline (Figure 2). The bending point of the coastline is located at $x = 800$ km and $y_c =$ 1,000 km. The surface roughness length over the land is set to 0.1 m.

The initial state is given by a uniform zonal wind $\overline{u}$ without vertical shear in an atmosphere with piecewise constant stratification

$$\overline{\theta} = \begin{cases} \theta_s + \Gamma_T z & (z \le z_T) \\ \theta_s + \Gamma_T z_T + \Gamma_S (z - z_T) & (z > z_T) \end{cases}, \qquad (25)$$

where Γ_T and Γ_S are the vertical potential temperature gradient in the troposphere and stratosphere, respectively, and z_T is the height of the tropopause. The surface potential temperature of land is fixed and identical to the potential temperature of the atmosphere at $z = 0$ m for the initial state. The choices for our model simulations are summarised in Table 1. The simulation is integrated for 96 hr, where the western and eastern boundary conditions are given by the initial state. Note that the eastern boundary conditions do not affect the inner domain due to the wind direction being outward.

TABLE 1 List of model parameters

Description	Symbol	Value
Zonal wind speed	$\overline{u}$	10 m s^{-1}
Height of tropopause	z_T	7 km
Vertical potential temperature gradient in the stratosphere	Γ_S	15 K km^{-1}
Potential temperature of the atmosphere at $z = 0$ m	θ_s	257.5 K
Average pressure at the surface	p_0	1,013 hPa
Reference potential temperature	θ_0	280 K
Basic state density	ρ_0	1 kg m^{-3}
Bulk coefficient for the surface sensible flux	c_H	1.4×10^{-3}
Friction coefficient	ν	1.0×10^{-3} s^{-1}

TABLE 2 List of parameters used in the numerical simulation. The values in parentheses correspond to the control experiment

Description	Symbol	Value
Angle of the bend in coastline	ϕ	30°, 60°, (90°), 120°, 150°
Vertical potential temperature gradient in the troposphere	Γ_T	4, (5), 6 K km^{-1}
Sea-surface temperature	θ_s	0, 5, (10), 15° C

We performed several dry experiments using different sets of Γ_T, SST, and ϕ. The set-up for the control experiment is $\Gamma_T = 5$ K km^{-1}, SST = 10°C, which are typical values for a CAO over the Japan Sea, and $\phi = 90°$. For the other experiments, we changed one of these parameters; see Table 2. In addition to the dry experiments, we also performed a moist experiment using the same parameters as for the dry control experiment, where the initial state has zero humidity.

4 | DRY EXPERIMENTS AND SENSITIVITY OF ANALYTIC SOLUTIONS

The control experiment features a convergence zone extending eastward from the bending point of the coastline (shading, Figure 3a). At the beginning of the simulation, the cold airmass originally located over the land migrates eastward, accompanied by convergence at its

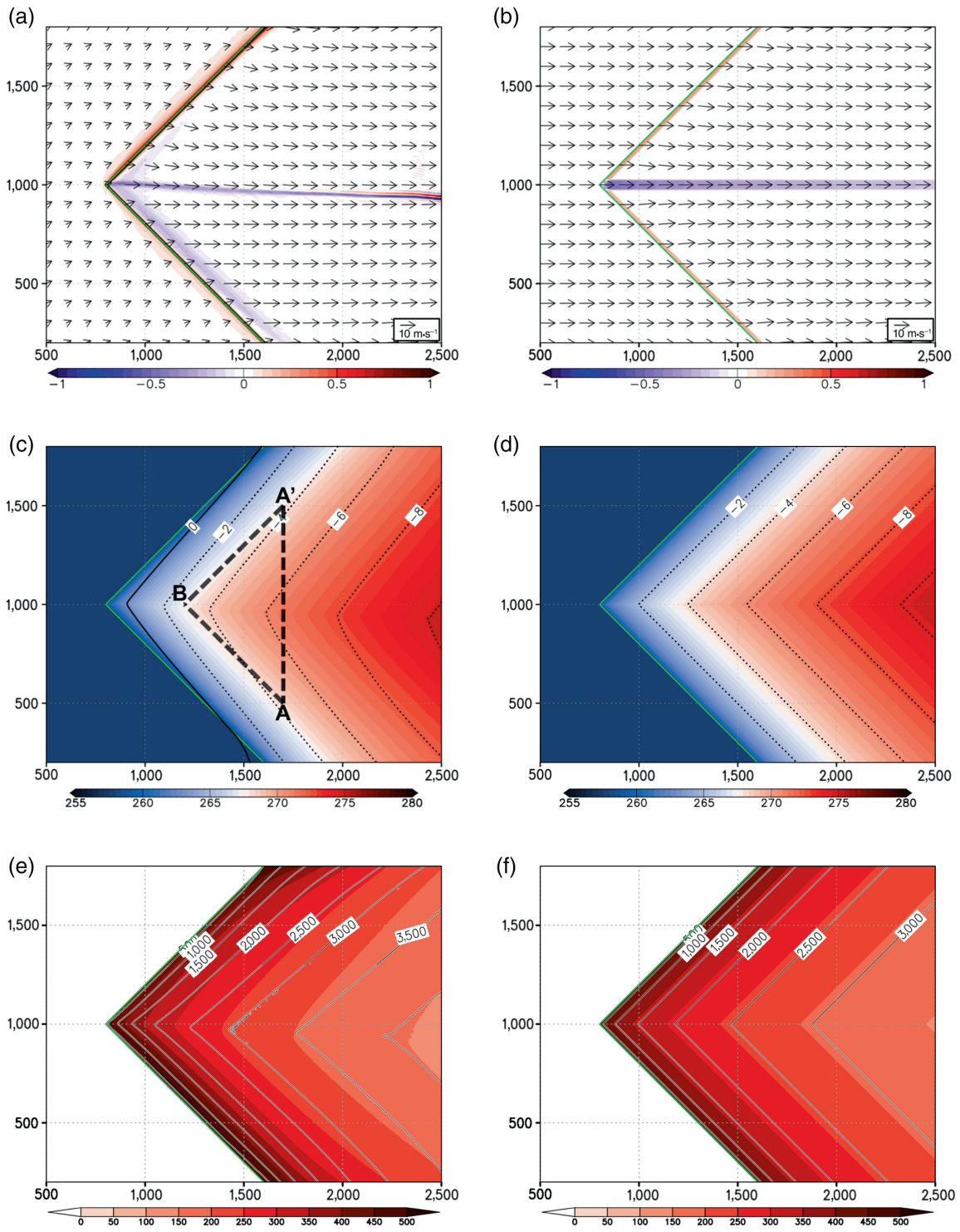

FIGURE 3 (a, b) Horizontal divergence (colour shading; $\times 10^{-4}$ s^{-1}) and horizontal wind vectors (arrows) at $z = 10$ m. (c, d) Potential temperature (colour shading; K) at $z = 10$ m and sea-level pressure deviation (positive and negative contours with an interval of 1 hPa are denoted by solid and dotted lines, respectively). (e, f) Surface sensible heat flux (colour shading; W·m^{-2}) and depth of the mixed layer (contour; interval 500 m), which is defined as the height of the upper end of a continuous layer of more than 1,000 m in which $S_{H2.5}$ is less than 0.01, where $S_{H2.5}$ appears in the expression of the turbulent diffusion coefficient in the Mellor–Yamada–Nakanishi–Niino scheme. Left panels: numerical model at $t = 96$ hr for the control experiment; right panels: analytic solution, where the divergence for the analytic solution is calculated assuming that the change of v occurs across a convergence zone of 50 km width centred at $y = y_c$. The green line indicates the coastline

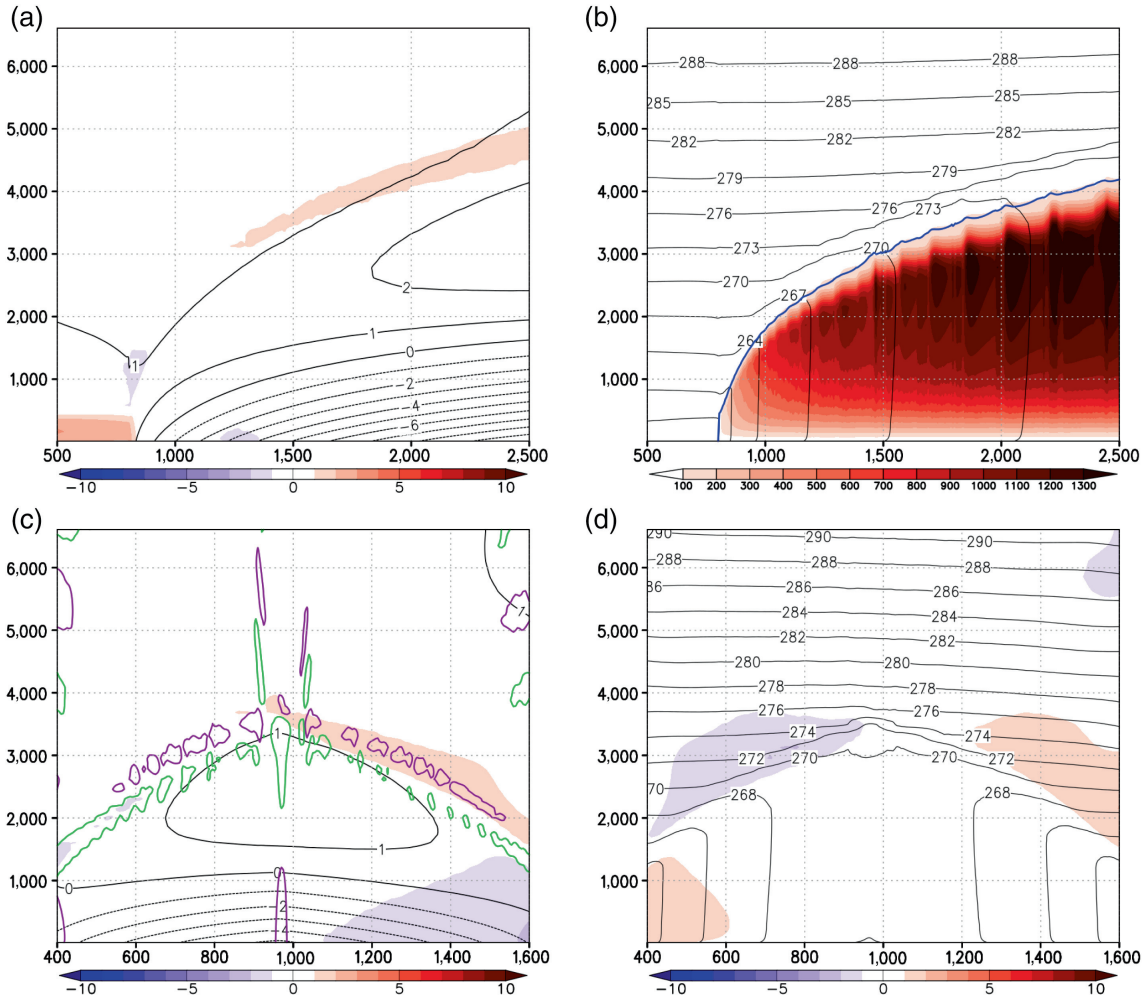

FIGURE 4 Vertical cross-section for the dry experiment at $t = 96$ hr. (a, b) At $y = y_c$ and (c, d) at $x = 1{,}500$ km. (a) Meridional wind (shading; $m \cdot s^{-1}$) and pressure perturbation (contour; hPa). (b) Potential temperature (contour; K) and turbulent diffusion coefficient for momentum (shading; $m^2 \cdot s^{-1}$). The blue contour indicates diagnosed boundary-layer depth. (c) Meridional wind (shading; $m \cdot s^{-1}$), pressure perturbation (contour; hPa), and divergence/convergence (green/purple contour, with 10^{-5} s^{-1}). (d) Potential temperature (contour; K), zonal wind perturbation (shading, $m \cdot s^{-1}$), and relative vertical vorticity (green contours, 10^{-5} s^{-1}, values too small to be in range)

leading edge. Behind the leading edge, the convergence zone develops from the bending point in the coastline. The convergence zone undulates slightly due to a fluctuation of the meridional wind caused by an initial shock. Once this fluctuation reaches the eastern boundary at about $t =$ 90 hr, the convergence zone becomes almost steady. In this steady state, the wind is almost zonal over the entire sea, except north of the convergence zone towards the coastline, where it has a slightly southward component (vectors, Figure 3a). This southward wind component is restricted to the lower levels, whereas northward wind is evident at the top of the mixed layer (shading, Figure 4a). Furthermore, the meridional wind components are only present on the northern side of the convergence zone (shading, Figure 4c). The width of the convergence zone is about 50 km, with a maximum convergence of about 3×10^{-5} s^{-1} at $x = 1{,}500$ km (shading, Figure 3a), corresponding to a $1\ m \cdot s^{-1}$ $\Delta v'$ discontinuity in the meridional wind across the convergence zone. The convergence zone features significant convergence up to 1,000 m, but the structure at the top of the mixed layer is more diffuse and features a dipole in the vertical (purple and green contour, Figure 4c).

In accordance with the large thermal land–sea contrast, the sensible heat fluxes near the coast are greater than $400\ W \cdot m^{-2}$ and gradually decrease with increasing fetch (shading, Figure 3e). Accordingly, potential temperature rises (shading in Figure 3c and contour in Figure 4b) in conjunction with mixed-layer depth (contours in Figure 3e and blue contour in Figure 4b). The mixed layer is characterised by significant turbulent vertical mixing (shading, Figure 4b) due to the turbulent energy in the boundary layer associated with the vertical redistribution of the surface sensible heat flux.

Owing to the bend in the coastline, potential temperature maximises along y_c in the centre of the domain, collocated with a trough in the sea-level pressure perturbation (contours, Figure 3c). Through hydrostatic balance, the pressure perturbation (contour, Figure 4a) is directly related to the increase of temperature and mixed-layer depth with fetch—see Equation (13)—in the CAO (Figure 4b). At the top of the mixed layer above the convergence zone, the isentropes are bending upwards (contour, Figure 4d), indicating a negative potential temperature anomaly that is collocated with an anticyclonic circulation evident in the zonal wind perturbation (Figure 4c,d).

The overall structure of the convergence zone, potential temperature, surface sensible heat flux, depth of the mixed layer, and pressure are consistent with the mechanism considered in the analytic model. Similar structures are found in the experiments with different ϕ (not shown). Using the bulk coefficient $c_H = 1.4 \times 10^{-3}$ and friction coefficient $\nu = 1.0 \times 10^{-3}\,\mathrm{s}^{-1}$ estimated from the numerical simulation, the analytic solution provides a very good prediction of the results of the numerical simulation (compare Figure 3b,d,f). In the analytic solution, the surface friction over the land is ignored. Therefore, the wind speed over land is higher in the analytic solution. Additionally, weak convergence near the southern coastline in the numerical simulation is also caused by the difference in the friction between land and sea. Note that the mixed layer in the numerical simulation is deeper than in the analytic solution (compare Figure 3e,f), which is most likely attributable to the entrainment at the top of the boundary layer associated with boundary-layer parametrisation and partially by the resolved overturning in the numerical model yielding a vertical overshooting at the top of the mixed layer.

In general, our results compare well with other idealised CAO simulations, such as the one by Spensberger and Spengler (2021). They used double the wind speed ($20\,\mathrm{m{\cdot}s^{-1}}$), but a lower air–sea contrast (16 K instead of 26 K in the default set-up here), resulting in similar surface heat fluxes. However, the development of the mixed layer is rather different between our study and theirs, with atmospheric mixed-layer depths almost twice as deep in our simulations. This discrepancy is due to the weaker stability in our simulations—$5\,\mathrm{K{\cdot}km^{-1}}$ compared with $8\,\mathrm{K{\cdot}km^{-1}}$ in Spensberger and Spengler (2021))—allowing for an accelerated growth of the mixed layer with fetch given similar surface fluxes.

To compare the analytic solution and the numerical simulation quantitatively, we contrast potential temperature at $z = 10\,\mathrm{m}$, meridional surface pressure gradient (dp'_s/dy) at $x = 1{,}500\,\mathrm{km}$, and the jump in meridional velocity $\Delta v'$ across the convergence zone at the location of maximum convergence for each experiment. The analytic solution reproduces the sensitivity of the potential temperature to the SST, Γ_T, and ϕ with high fidelity (Figure 5a–c). Higher SSTs cause higher surface sensible heat fluxes, and thus higher potential temperature (Figure 5a). There is a slight geographic asymmetry between the numerical simulation and the analytic model, with the maximum in potential temperature shifted exceedingly southward off the centre at $y_c = 1{,}000\,\mathrm{km}$ with increasing SST. This asymmetry is also evident in the slight southward displacement of the convergence zone (shading, Figure 3a). This asymmetry will be discussed in more detail in Section 5.

The sensitivity to Γ_T is relatively weak, with the potential temperature in the mixed layer increasing more rapidly for larger Γ_T (Figure 5b). This is associated with higher Γ_T featuring a shallower mixed layer, whereby the heat provided by the surface fluxes is more efficiently heating the mixed layer and yielding higher temperatures.

When varying ϕ, the effect of the varying fetch across the different experiments becomes apparent, with meridional potential temperature gradients becoming larger for smaller ϕ (Figure 5c). Note that the potential temperature at the centre of the domain for $\phi = 30°$ in the numerical simulation is slightly lower than for the analytic solution. This is most likely associated with more significant meridional temperature advection into the centre of the domain and horizontal mixing in a rather narrow CAO.

Through hydrostatic balance, the potential temperature distribution results in a meridional gradient of hydrostatic perturbation pressure directed to the convergence zone in the centre of the domain, where the sign of the gradient of perturbation pressure changes abruptly. Although the jump of the gradient of the pressure perturbation in the numerical simulation is smaller than in the analytic solution, the behaviour of the gradient of the pressure perturbation for different SST, Γ_T, and ϕ is qualitatively similar, with the meridional perturbation pressure gradient on either side of the convergence zone being larger for higher SST, smaller Γ_T, and smaller ϕ (Figure 5d–f).

These sensitivities of the perturbation pressure gradient (Figure 5d–f) can be related to the gradients in potential temperature (Figure 5a–c). The meridional temperature gradient is larger for higher SST (Figure 5a), resulting in stronger pressure gradients (Figure 5d). This is related to the air masses experiencing a relatively stronger surface heating at higher SST and thereby featuring higher potential temperatures with fetch as well as deeper mixed layers. Both act to increase the surface pressure perturbation—see Equation (13).

On the other hand, Γ has relatively little effect (Figure 5e), as there are competing effects associated with changes in stability. As previously indicated, larger

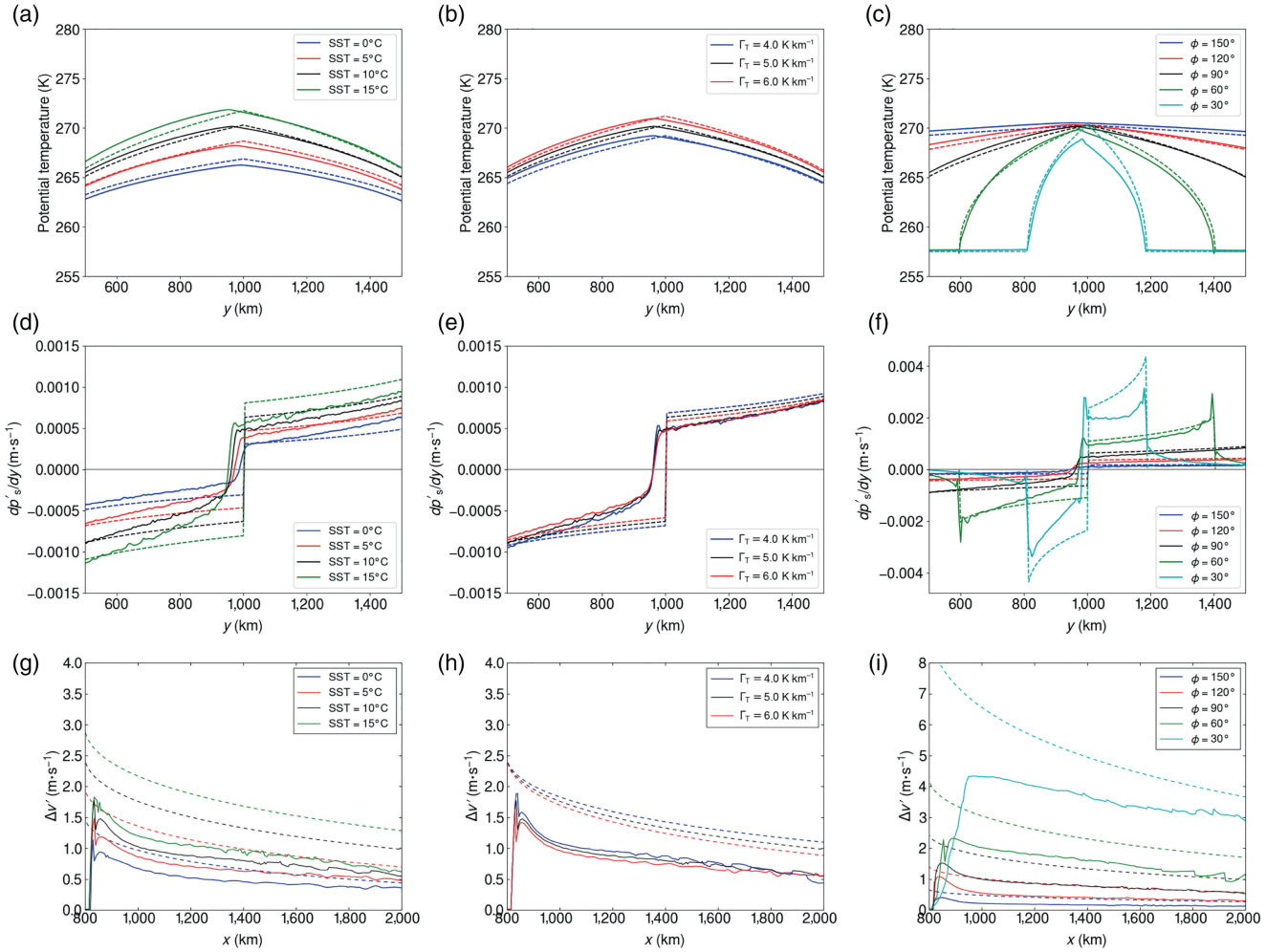

FIGURE 5 (a) Potential temperature at $x = 1{,}500$ km at $z = 10$ m for different sea-surface temperatures (SSTs); (b) and (c): same as (a) except for different Γ_T and different ϕ, respectively. Dashed and solid lines indicate the analytic solution and numerical simulation, respectively. (d), (e) and (f): same as (a), (b), and (c), respectively, except for dp'_s/dy. (g), (h), and (i): same as (a), (b), and (c), respectively, but for jump of v at the centre of the domain in the analytic model (dashed line) and the numerical simulations (solid line). For the numerical experiment, the jump is defined as the difference of v between 25 km to the north and south of the location of the maximum convergence

Γ yields higher potential temperatures due to reduced mixed-layer depths. Hydrostatically, the higher temperature is thus compensated by the reduced mixed-layer depth over which one has to integrate to obtain the surface pressure perturbation—see Equation (13). For the given set-up, it appears that the effect associated with the growths of the mixed-layer depth for smaller Γ outweighs the potential temperature effect for higher Γ, resulting in a stronger meridional pressure gradient for less stable environments (Figure 5e).

Defining the jump of v' ($\Delta v'$) at the centre of the domain as the difference of v between 25 km to the north and south from the line of the maximum convergence in the numerical experiment, we can compare the results with the analytic solution (Figure 5g–i). Although the analytic solution overestimates $\Delta v'$ due to the larger jump of the meridional pressure gradient and the assumption of the fixed width of the convergence zone for the simulation, the qualitative characteristics are similar. In contrast to the analytic solution, the numerical model features very weak convergence near the coastline and asymptotes towards the analytic solution with fetch. Note the caveat of the definition of $\Delta v'$ in the numerical experiment for small fetch, where the location 25 km to the north and south of the convergence zone is over land. Downstream of the coastline or ice edge, $\Delta v'$ is larger for higher SST, smaller Γ_T, and smaller ϕ, which is consistent with the sensitivity of meridional pressure gradients explained earlier (Figure 5d,e). Therefore, the analytic solution reasonably explains the formation mechanism of the convergence zone associated with the bend in the coastline or sea-ice edge.

As indicated, some of the disagreements between the analytic solution and the numerical simulation are most

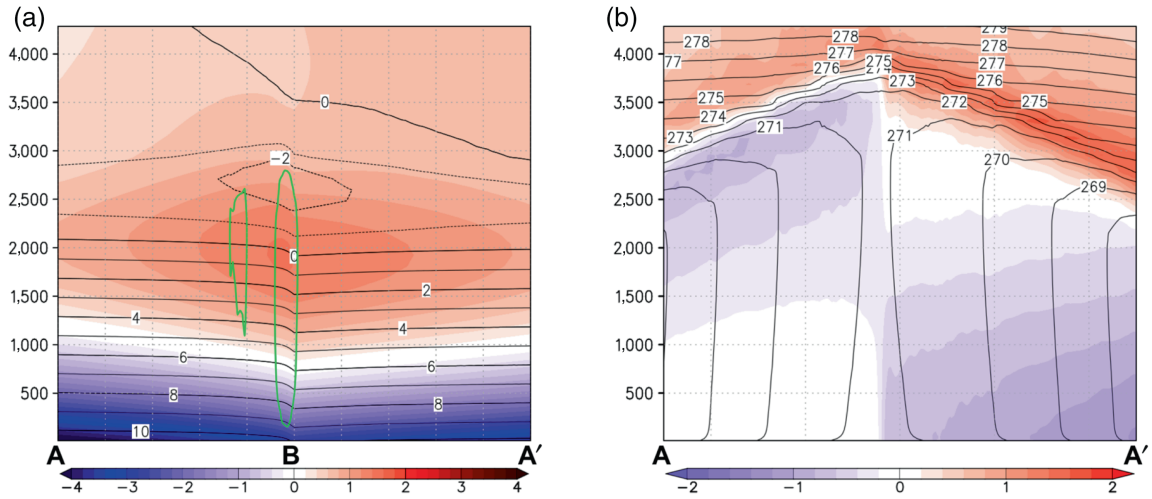

FIGURE 6 Vertical cross-section for the dry experiment at $t = 96$ hr. (a) Pressure deviation (shading; hPa), potential temperature deviation (contour; interval 1 K), and vertical velocity (green contours, 0.05 $m \cdot s^{-1}$) along A–B–A′ in Figure 3c. (b) Meridional wind (shading) and potential temperature (contour; interval 1 K) along A–A′ in Figure 3c

likely associated with the underlying assumptions for the analytic model, such as the neglect of meridional advection. Other discrepancies are also due to the limitations of the analytic model. For example, resolved vertical motion is neglected in the analytic solutions. Vertical motion in the numerical model (green contour, Figure 6a), however, can be associated with a negative potential temperature anomaly in the vertical cross-section at the top of the mixed layer, which is caused by the adiabatic cooling associated with the overshooting of the updraft (Figure 6b). However, this anomaly is not uniform and largest along the centre of the domain, even in a cross-section with the same fetch (A–B–A′, Figure 6a), because the updraft maximises there in correspondence with the convergence zone. This negative potential temperature anomaly suppresses the amplitude of the negative pressure perturbation at the surface through the hydrostatic relation in Equation (13) (Figure 6a), yielding a weaker meridional pressure gradient in the numerical simulation compared with the analytic solution (Figure 5d–f).

5 | EXPERIMENT INCLUDING MOIST PROCESSES

Although we showed that convergence zones can form in a dry atmosphere, observed convergence zones are usually accompanied by a cloud band with latent heat release. To evaluate the effect of latent heat release on the evolution of convergence zones, we performed a moist experiment using the same parameters as the control experiment (see Tables 1 and 2), where we prescribed the same dry atmosphere at the initial time and upstream boundary as in the control experiment. Thus, water vapour is only supplied via latent heat fluxes from the sea surface. We have also carried out a moist experiment with a horizontal grid spacing of 2 km and without a convection parametrisation scheme. The result of this experiment was qualitatively similar to the experiment with a horizontal grid spacing of 5 km with convection parametrisation scheme.

The effect of the latent heat release is readily evident in the convective structure in the low-level divergence and vorticity that sets in around 300–500 km downstream of the coastline (shading, Figure 7a,b). Furthermore, the vertically integrated latent heating features banded structures representative of cloud streets typically forming in CAOs (shading, Figure 7d). The latent heating also contributes to additional warming within the cloud layer of the CAO (green contour, Figure 8b), which yields a moist adiabatic stratification and thus increasing potential temperature (black contour) with altitude in the cloud layer above the diagnosed mixed-layer depth (blue contour). Note that the diagnosed mixed-layer depth in the moist experiment is much shallower than in the dry experiment (blue contour, Figure 4b), because the potential temperature increases with altitude above the level of free convection. Therefore, the turbulent diffusion (shading, Figure 8b) is strongest in the part of the CAO between the coastline and the onset of convection, whereas it is suppressed once convection sets in because the convection then takes on the dominant role for vertical heat transport.

Both the low-level divergence and vorticity (shading, Figure 7a,b) have a much richer structure than in the dry experiment (Figure 3a), where the moist experiment features the aforementioned transition around 300–500 km downstream from the coastline associated with the onset

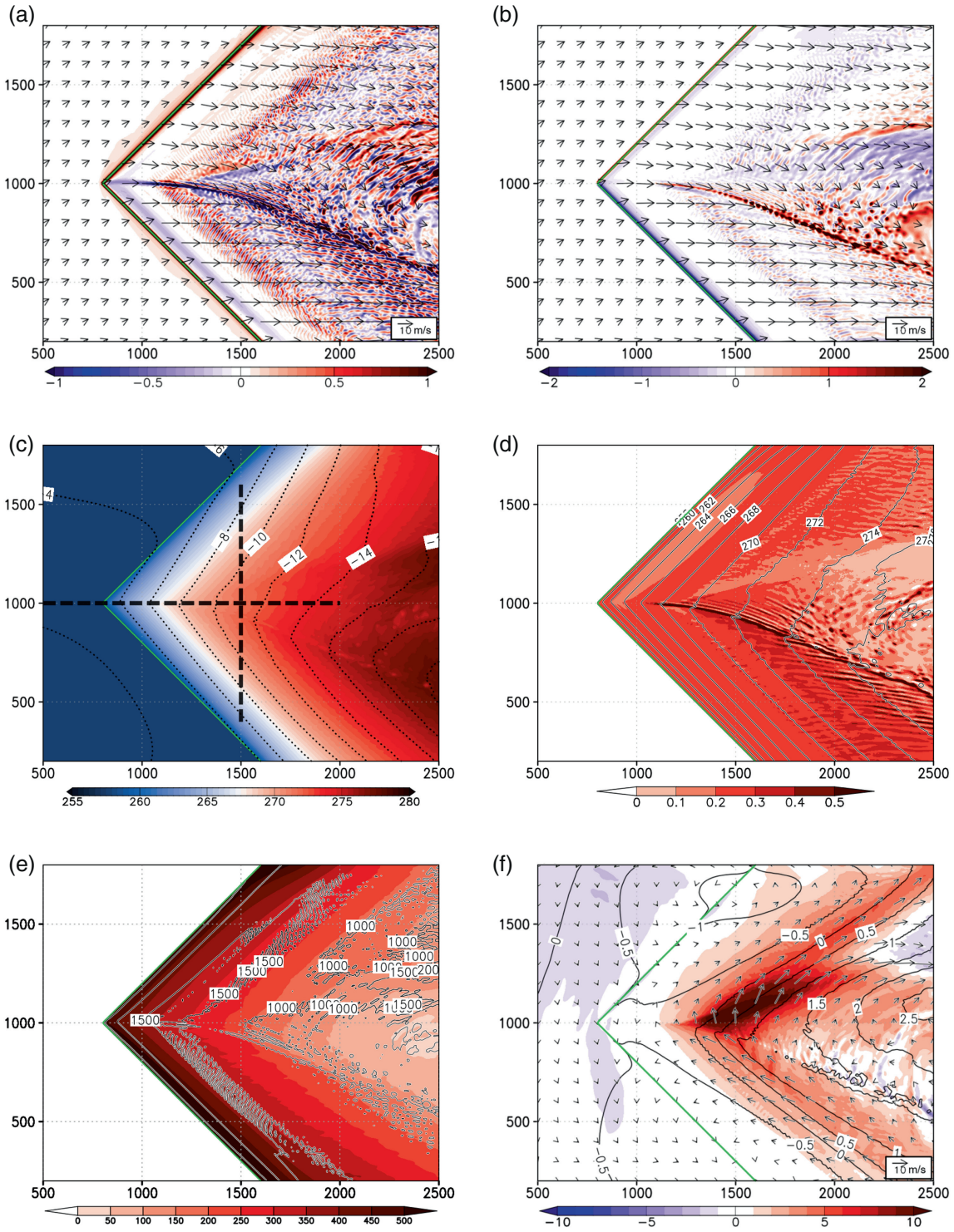

FIGURE 7 (a, c, e) Same as Figure 3 but for the moist experiment. (a) Horizontal divergence (colour shading; $\times 10^{-4}$ s^{-1}) and horizontal wind vectors (arrows) at $z = 10$ m. (b) Relative vorticity (colour shading; $\times 10^{-4}$ s^{-1}) and horizontal wind vectors (arrows) at $z = 10$ m. (c) Potential temperature (colour shading; K) at $z = 10$ m and sea-level pressure deviation (positive and negative contours with an interval of 1 hPa are denoted by solid and dotted lines, respectively). (d) Vertically averaged diabatic heating (colour shading; K·h^{-1}) and potential temperature at $z = 10$ m (contour; interval is 2 K). (e) Surface sensible heat flux (colour shading; W·m^{-2}) and depth of the mixed layer (contour; interval 500 m). (f) Meridional wind (colour shading; m·s^{-1}), pressure deviation (contour; interval is 0.5 hPa), and horizontal perturbation wind vectors (arrows) at $z = 3{,}495$ m. Thick dashed lines in (c) indicate the locations of the cross-sections in Figure 8.

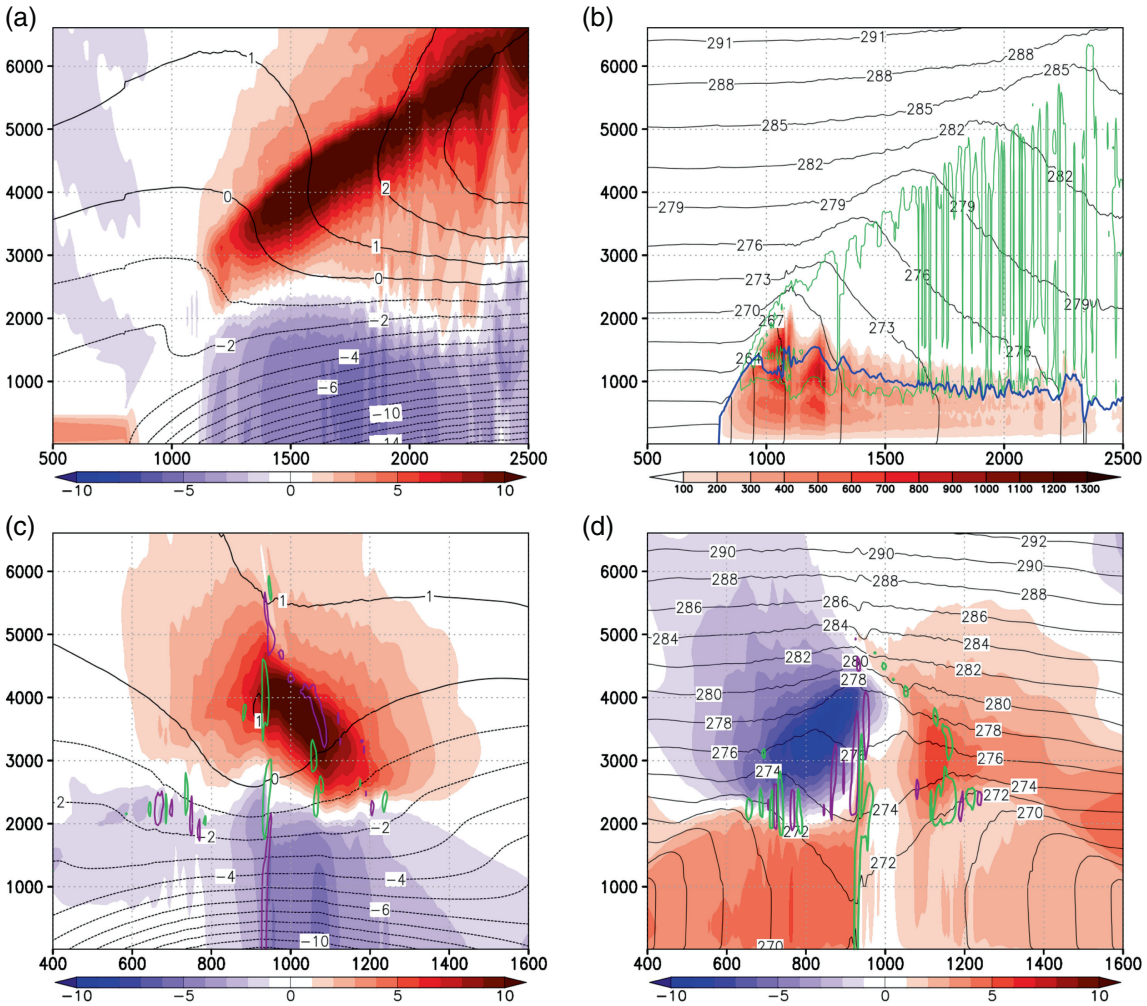

FIGURE 8 Same vertical cross-section as Figure 4 at $t = 96$ hr, but for the moist experiment. (a, b) At $y = y_c$ and (c, d) at $x = 1{,}500$ km. (a) Meridional wind (shading; $m \cdot s^{-1}$) and pressure perturbation (contour; hPa). (b) Potential temperature (contour; K), turbulent diffusion (shading; $m^2 \cdot s^{-1}$), and latent heat release (green contour, 0.1 $K \cdot hr^{-1}$). The blue contour indicates diagnosed boundary-layer depth. (c) Meridional wind (shading; $m \cdot s^{-1}$), pressure perturbation (contour; hPa), and divergence/convergence (green/purple contour, with 10^{-4} s^{-1}). (d) Potential temperature (contour; K), zonal wind perturbation (shading, $m \cdot s^{-1}$), and relative vertical vorticity (green/purple contours, for positive/negative values, 10^{-4} s^{-1})

of convection. The convection is evident in the speckled structure in both divergence and vertical vorticity and maximises along the convergence zone. Further downstream, the convective plumes appear to conglomerate into larger cells and start to become more organised. The fact that several of the convective plumes have significant vorticity associated with them (shading, Figure 7b) indicates that some of the updrafts might feature rotation or enhanced horizontal shear along their boundaries.

Similar to the dry experiment, the convergence zone in the moist experiment is collocated with the potential temperature maximum (shading, Figure 7c). The surface pressure perturbation (contour) resembles the structure of the potential temperature, indicating a high degree of hydrostatic balance, which is evident when comparing the vertical cross-sections of perturbation pressure and potential temperature (contours in Figure 8a,b). Thus, similar to the dry experiment and as postulated in the analytic model, the trough in the moist experiment is also directly linked to the vertically integrated potential temperature perturbation.

The convergence zone in the moist experiment is significantly stronger than in the dry experiment (compare Figures 3a and 7a), with maximum convergence at $x = 1{,}500$ km being 4.0×10^{-4} s^{-1}, which is more than 10 times as large as that in the dry experiment. This difference is due to a feedback mechanism, where the convergence zone triggers moist convection, leading to latent heat release that intensifies the updraft and resulting in a further intensification of the low-level convergence. Furthermore, the convergence zone in the moist experiment is accompanied by a strong horizontal wind shear with a maximum

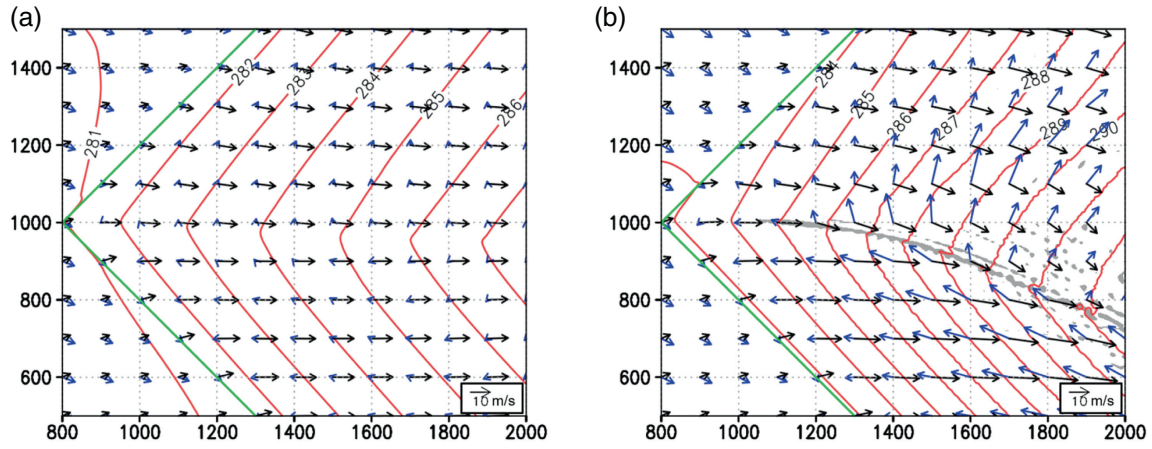

FIGURE 9 Potential temperature averaged between $z = 10$ m and $z = 3{,}495$ m (red contour; interval 1 K), horizontal wind vectors at $z = 10$ m (black arrows), and difference in the wind vectors between $z = 3{,}495$ m and $z = 10$ m (blue arrows) at $t = 96$ hr for the (a) dry and (b) moist experiment. Grey shading indicates the area with horizontal divergence at $z = 10$ m larger than 1×10^{-4} s^{-1}. The green line indicates the coastline

relative vorticity of about 2.0×10^{-4} s^{-1} at $x = 1{,}500$ km (Figure 7b), whereas low-level horizontal wind shear is more or less absent in the dry experiment (contour out of range, Figure 4d). This discrepancy can also be explained by the enhanced updraft, which intensifies the relative vorticity through stretching of both planetary and relative vorticity associated with the weak horizontal wind shear caused by the dry mechanism.

The enhanced warming in the cloud layer associated with the latent heating also contributes to the observed intensity of the convergence zone in the moist experiment. Compared with the dry experiment (contour, Figure 4b), the potential temperature above 1,000 m is higher in the moist experiment due to the additional heating from condensation (contour, Figure 8b). Even the mixed layer underneath the cloud base is significantly warmer in the moist experiment than in the dry experiment. In addition, the depth of the layer in which the airmass transformation takes place has a higher vertical extent in the moist experiment due to the additional heat release in the cloud layer. Thus, consistent with the hydrostatic relation for the surface pressure perturbation in Equation (13), both a higher temperature and a deeper layer over which the airmass transformation takes place contribute to an enhanced surface pressure perturbation in the moist experiment, yielding a stronger convergence.

The convergence zone in the moist experiment bends significantly southward from the centreline starting around 300 km downstream from the bend in the coastline (shading, Figure 7a). The beginning of the deflection also marks the onset of convection (green contours, Figure 8b) and the position where the low-level horizontal wind shear (shading, Figure 7b), integrated diabatic heating (shading, Figure 7d), and meridional wind at the top of the mixed layer (shading, Figures 7f and 8a) increase significantly. The negative (positive) zonal gradient of perturbation pressure at the lower (upper) levels is associated with significant geostrophic northerlies (southerlies) (Figures 7f and 8a,c). Note that the convergence zone in the dry experiment only features a weak southward deflection despite similar zonal perturbation pressure gradients (shading, Figure 3a). This is due to turbulent mixing of momentum dominating over the Coriolis force, rendering the low-level wind highly ageostrophic (Figure 4a,b).

The enhanced heating along the leading edge of the onset of convection around 1,200 km yields an increase in the temperature gradient in the x-direction (shading, Figure 7d), equivalent to a diabatic frontogenetic forcing. This diabatic frontogenetic forcing is associated with a thermally direct overturning circulation through the Sawyer–Eliassen equation (Sawyer, 1956; Eliassen, 1962). This overturning circulation, in turn, continuously aims to attain thermal wind balance given the enhancing temperature gradient associated with the latent heat release. This thermal wind is evident in the meridional wind shear across the centre of the domain, with northward flow at the upper levels and southward flow at the lower levels (shading, Figure 8a,c; blue vectors, Figure 9b). In addition, owing to the geometry of the coastline, and thus the geometry of the onset of convection, the thermal wind also projects onto the zonal wind perturbation, yielding an anticyclonic circulation at upper levels around the cloud layer of the CAO (shading, Figure 8d; blue vectors, Figure 9b).

The wind speed is reduced at lower levels compared with upper levels due to the turbulent mixing of momentum below the cloud layer and surface friction. Therefore, the larger scale circulation is barely visible in the

below-cloud layer of the CAO. The latter reasoning also explains why the vertical wind shear vector does not align with the mixed-layer isotherms (blue vectors and red contours, Figure 9a), because the turbulent mixing suppresses geostrophic adjustment and thus yields a significant deviation from thermal wind. In addition, low-level convergence and upper-level divergence associated with the convergence zone intensify (weaken) the vertical shear of the meridional wind to the north (south) of the convergence zone (Figure 8c).

Associated with this asymmetry, the vertical shear of the horizontal wind features a strong asymmetry across the convergence zone for the moist experiment, which is much less pronounced in the dry experiment (blue vectors, Figure 9). The wind shear vectors for the moist experiment are almost perpendicular to the low-level wind (black vectors) to the north of the convergence zone, whereas they are antiparallel to the south of the convergence zone. This asymmetry in vertical shear is consistent with the observed vertical shear around the JPCZ (Murakami, 2019), which causes the transverse and longitudinal alignment of the cloud streets, respectively (Figure 1a), even though our numerical simulation cannot resolve the roll convection due to the coarse horizontal resolution. Note that the mid-level weak wind zone pointed out by Nagata (1992), which is produced by rapid vertical displacement with diabatic heating in a sheared environment, does not form in our experiment because we assume a uniform basic zonal flow without vertical shear.

6 | DISCUSSION AND CONCLUDING REMARKS

We used analytic solutions and numerical simulations to investigate how a bend in a coastline or sea-ice edge affects the formation of convergence zones in maritime CAOs. Our analytic solution explains the fundamental formation mechanism of convergence zones in CAOs associated with a bend in the coastline, where a warm wedge forms downstream of the bend due to the difference in the fetch over the relatively warmer sea. A hydrostatic pressure trough is collocated with the warm wedge and causes frictional convergence. The analytic solutions confirmed that a stronger convergence zone forms for higher SST, a less stable atmosphere, and a smaller angle of the bend in the coastline or sea-ice edge.

The dry numerical experiments show that the analytic solutions explain the near-surface temperature distribution but highlight some disagreement in the surface pressure distribution. The latter is due to the limitation of the analytic model, which does not consider the adiabatic cooling associated with the overshooting updraft above the convergence zone and meridional advection of potential temperature within the CAO.

In contrast to previous studies that mainly attributed the formation of maritime convergence zones to thermal variations in the lower boundary (e.g., land–sea contrast or a favourable SST distribution; Atlas *et al.*, 1983; Nagata *et al.*, 1986; Nagata, 1991), we demonstrated that the main cause of formation is attributable to a difference in fetch within CAOs. The difference in fetch for bent coastlines or sea-ice edges causes a non-uniform airmass transformation that results in the formation of a convergence zone. This mechanism explains the occurrence of convergence zones over both closed and open water bodies.

We find that the wind direction and sea-surface heat fluxes are important factors for the formation of the convergence zone, which is consistent with Norris *et al.* (2013) and Mazon *et al.* (2015), who found that convergence zones tend to occur when the wind is strong and parallel to the long axis of the water body and when the air–sea temperature difference is large, indicating the potential for large surface heat fluxes.

Although we find that a convergence zone can form in a dry atmosphere, the convergence is intensified by an order of magnitude when moist processes are included. This intensification is due to a feedback process, where the convection triggered along the convergence zone releases latent heat, thereby intensifying the updraft that in turn enhances the horizontal convergence.

Another difference between the dry and moist simulations is the formation process of the warm wedge and associated pressure trough. In the dry simulation, the warm wedge, caused only by the turbulent heat transport, exists only in the boundary layer, where turbulent momentum mixing is dominant over the Coriolis force. Thus, the meridional geostrophic circulation associated with the zonal gradient of the pressure perturbation is small. In the moist experiment, on the other hand, the warm wedge and pressure perturbation are also present in the free atmosphere due to latent heat release, where the Coriolis force is dominant. The negative zonal gradient of the pressure perturbation causes a southward geostrophic flow in the lower atmosphere that deflects the convergence zone southward.

Furthermore, the moist simulation features an asymmetry in the vertical shear of the horizontal wind across the convergence zone. The vertical shear vector is perpendicular and antiparallel to the low-level wind to the north and south of the convergence zone, respectively. This is consistent with the observed asymmetry in the vertical shear yielding the transverse and longitudinal alignment of the cloud streets, respectively, around the JPCZ (Murakami, 2019), in accordance with the linear theory of thermal convection in a vertical shear flow (Asai, 1972). This asymmetry in the vertical shear observed in our

simulation can be interpreted as the superposition of the thermal wind and the divergent flow associated with the convergence zone.

Our analytic model convincingly demonstrates that an asymmetry in the airmass transformation associated with the difference in the fetch is probably the major cause for convergence zones in CAOs. Additional factors, such as vertical wind shear, horizontal temperature gradients, varying SSTs, and topography over land can yield additional asymmetries in the airmass transformation that can modulate or cause a convergence zone. Our study thus provides a sound basis to further investigate the role of the other processes in the formation of convergence zones.

AUTHOR CONTRIBUTIONS

Shun-ichi I. Watanabe: conceptualization; formal analysis; investigation; methodology; visualization; writing – original draft. **Hiroshi Niino:** supervision; validation; writing – review and editing. **Thomas Spengler:** supervision; validation; writing – review and editing.

ACKNOWLEDGEMENTS

Shun-ichi I. Watanabe was supported by JSPS KAKENHI grant numbers 17K14390, 21H01164 and 19K03967. Hiroshi Niino was supported by MEXT Program for Promoting Researches on the Supercomputer Fugaku (Large Ensemble Atmospheric and Environmental Prediction for Disaster Prevention and Mitigation). The collaboration between the authors for this article was established through the Research Council of Norway project NORPAN (250135). We acknowledge the use of imagery from the NASA Worldview application (https://worldview.earthdata.nasa.gov), part of the NASA Earth Observing System Data and Information System (EOSDIS).

ORCID

Shun-ichi I. Watanabe https://orcid.org/0000-0003-4456-3932

REFERENCES

Andersson, T. and Gustafsson, N. (1994) Coast of departure and coast of arrival: Two important concepts for the formation and structure of convective snowbands over seas and lakes. *Monthly Weather Review*, 122(6), 1036–1049. https://doi.org/10.1175/1520-0493(1994)122<1036:codaco>2.0.co;2.

Asai, T. (1965) A numerical study of the air-mass transformation over the Japan Sea in winter. *Journal of the Meteorological Society of Japan. Series II*, 43(1), 1–15. https://doi.org/10.2151/jmsj1965.43.1_1.

Asai, T. (1972) Thermal instability of a shear flow turning the direction with height. *Journal of the Meteorological Society of Japan. Series II*, 50(6), 525–532.

Asai, T. (1988) Mesoscale features of heavy snowfalls in Japan Sea coastal regions of Japan. *Tenki*, 35, 156–161. (In Japanese).

Atkinson, B.W. and Zhang, J.W. (1996) Mesoscale shallow convection in the atmosphere. *Reviews of Geophysics*, 34(4), 403–431. https://doi.org/10.1029/96rg02623.

Atlas, D., Chou, S.-H. and Byerly, W.P. (1983) The influence of coastal shape on winter mesoscale air–sea interaction. *Monthly Weather Review*, 111(2), 245–252. https://doi.org/10.1175/1520-0493(1983)111<0245:tiocso>2.0.co;2.

Beljaars, A.C.M. (1995) The parametrization of surface fluxes in large-scale models under free convection. *Quarterly Journal of the Royal Meteorological Society*, 121(522), 255–270. https://doi.org/10.1002/qj.49712152203.

Beljaars, A.C.M. and Holtslag, A.A.M. (1991) Flux parameterization over land surfaces for atmospheric models. *Journal of Applied Meteorology*, 30(3), 327–341. https://doi.org/10.1175/1520-0450(1991)030<0327:fpolsf>2.0.co;2.

Burke, C.J. (1945) Transformation of polar continental air to polar maritime air. *Journal of Meteorology*, 2(2), 94–112. https://doi.org/10.1175/1520-0469(1945)002<0094:TOPCAT>2.0.CO;2.

Eito, H., Murakami, M., Muroi, C., Kato, T., Hayashi, S., Kuroiwa, H. and Yoshizaki, M. (2010) The structure and formation mechanism of transversal cloud bands associated with the japan-sea polar-airmass convergence zone. *Journal of the Meteorological Society of Japan*, 88(4), 625–648. https://doi.org/10.2151/jmsj.2010-402.

Eliassen, A. (1962) On the vertical circulation in frontal zones. *Geofysiske Publikasjoner*, 24(4), 147–160.

Ikawa, M., Mizuno, H., Matsuo, T., Murakami, M., Yamada, Y. and Saito, K. (1991) Numerical modeling of the convective snow cloud over the Sea of Japan precipitation mechanism and sensitivity to ice crystal nucleation rates. *Journal of the Meteorological Society of Japan*, 69(6), 641–667. https://doi.org/10.2151/jmsj1965.69.6_641.

Japan Meteorological Agency (2013) *Outline of the operational numerical weather prediction at the Japan Meteorological Agency*. http://www.jma.go.jp/jma/jma-eng/jma-center/nwp/outline2013-nwp/index.htm.

Kain, J.S. (2004) The Kain–Fritsch convective parameterization: An update. *Journal of Applied Meteorology*, 43(1), 170–181. https://doi.org/10.1175/1520-0450(2004)043<0170:tkcpau>2.0.co;2.

Kain, J.S. and Fritsch, J.M. (1990) A one-dimensional entraining/detraining plume model and its application in convective parameterization. *Journal of the Atmospheric Sciences*, 47(23), 2784–2802. https://doi.org/10.1175/1520-0469(1990)047<2784:aodepm>2.0.co;2.

Laird, N.F., Metz, N.D., Gaudet, L., Grasmick, C., Higgins, L., Loeser, C. and Zelinsky, D.A. (2017) Climatology of cold season lake-effect cloud bands for the North American Great Lakes. *International Journal of Climatology*, 37(4), 2111–2121. https://doi.org/10.1002/joc.4838.

Laird, N.F., Walsh, J.E. and Kristovich, D.A.R. (2003) Model simulations examining the relationship of lake-effect morphology to lake shape, wind direction, and wind speed. *Monthly Weather Review*, 131(9), 2102–2111. https://doi.org/10.1175/1520-0493(2003)131<2102:msetro>2.0.co;2.

Mazon, J., Niemelä, S., Pino, D., Savijärvi, H. and Vihma, T. (2015) Snow bands over the Gulf of Finland in wintertime. *Tellus A: Dynamic Meteorology and Oceanography*, 67(1), 25102. https://doi.org/10.3402/tellusa.v67.25102.

Michel, C., Terpstra, A. and Spengler, T. (2018) Polar mesoscale cyclone climatology for the Nordic Seas based on ERA-Interim. *Journal of Climate*, 31(6), 2511–2532. https://doi.org/10.1175/JCLI-D-16-0890.1.

Murakami, M. (2019) Inner structures of snow clouds over the Sea of Japan observed by instrumented aircraft: A review. *Journal of the Meteorological Society of Japan*, 97(1), 5–38. https://doi.org/10.2151/jmsj.2019-009.

Nagata, M. (1987) On the structure of a convergent cloud band over the Japan Sea in winter; a prediction experiment. *Journal of the Meteorological Society of Japan. Series II*, 65(6), 871–883.

Nagata, M. (1991) Further numerical study on the formation of the convergent cloud band over the Japan Sea in winter. *Journal of the Meteorological Society of Japan*, 69(3), 419–428.

Nagata, M. (1992) Modeling case study of the Japan-Sea convergent cloud band in a varying large-scale environment. *Journal of the Meteorological Society of Japan*, 70(1B), 649–671. https://doi.org/10.2151/jmsj1965.70.1B_649.

Nagata, M., Ikawa, M., Yoshizumi, S. and Yoshida, T. (1986) On the formation of a convergent cloud band over the Japan Sea in winter; numerical experiments. *Journal of the Meteorological Society of Japan. Series II*, 64(6), 841–855.

Nakanishi, M. and Niino, H. (2006) An improved Mellor–Yamada level-3 model: Its numerical stability and application to a regional prediction of advection fog. *Boundary-Layer Meteorology*, 119(2), 397–407. https://doi.org/10.1007/s10546-005-9030-8.

Norris, J., Vaughan, G. and Schultz, D.M. (2013) Snowbands over the English Channel and Irish Sea during cold-air outbreaks. *Quarterly Journal of the Royal Meteorological Society*, 139(676), 1747–1761. https://doi.org/10.1002/qj.2079.

Papritz, L. and Spengler, T. (2017) A Lagrangian climatology of wintertime cold air outbreaks in the Irminger and Nordic Seas and their role in shaping air–sea heat fluxes. *Journal of Climate*, 30(8), 2717–2737. https://doi.org/10.1175/jcli-d-16-0605.1.

Renfrew, I.A., Pickart, R.S., Våge, K., Moore, G.W.K., Bracegirdle, T.J., Elvidge, A.D., Jeansson, E., Lachlan-Cope, T., McRaven, L.T., Papritz, L., Reuder, J., Sodemann, H., Terpstra, A., Waterman, S., Valdimarsson, H., Weiss, A., Almansi, M., Bahr, F., Brakstad, A., Barrell, C., Brooke, J.K., Brooks, B.J., Brooks, I.M., Brooks, M.E., Bruvik, E.M., Duscha, C., Fer, I., Golid, H.M., Hallerstig, M., Hessevik, I., Huang, J., Houghton, L., Jónsson, S., Jonassen, M., Jackson, K., Kvalsund, K., Kolstad, E.W., Konstali, K., Kristiansen, J., Ladkin, R., Lin, P., Macrander, A., Mitchell, A., Olafsson, H., Pacini, A., Payne, C., Palmason, B., Pérez-Hernández, M.D., Peterson, A.K., Petersen, G.N., Pisareva, M.N., Pope, J.O., Seidl, A., Semper, S., Sergeev, D., Skjelsvik, S., Søiland, H., Smith, D., Spall, M.A., Spengler, T., Touzeau, A., Tupper, G., Weng, Y., Williams, K.D., Yang, X. and Zhou, S. (2019) The Iceland Greenland Seas Project. *Bulletin of the American Meteorological Society*, 100, 1795–1817. https://doi.org/10.1175/BAMS-D-18-0217.1.

Saito, K., Fujita, T., Yamada, Y., Ishida, J.-i., Kumagai, Y., Aranami, K., Ohmori, S., Nagasawa, R., Kumagai, S., Muroi, C., Kato, T., Eito, H. and Yamazaki, Y. (2006) The operational JMA nonhydrostatic mesoscale model. *Monthly Weather Review*, 134(4), 1266–1298. https://doi.org/10.1175/mwr3120.1.

Savijärvi, H.I. (2012) Cold air outbreaks over high-latitude sea gulfs. *Tellus A: Dynamic Meteorology and Oceanography*, 64(1), 12244. https://doi.org/10.3402/tellusa.v64i0.12244.

Savijärvi, H. (2015) Cold air outbreaks along a non-frozen sea channel: Effects of wind on snow bands. *Meteorology and Atmospheric Physics*, 127(4), 383–391. https://doi.org/10.1007/s00703-015-0370-8.

Sawyer, J.S. (1956) The vertical circulation at meteorological fronts and its relation to frontogenesis. *Proceedings of the Royal Society of London Series A*, 234, 346–362.

Sergeev, D., Renfrew, I.A. and Spengler, T. (2018) Modification of polar low development by orography and sea ice. *Monthly Weather Review*, 146(10), 3325–3341. https://doi.org/10.1175/mwr-d-18-0086.1.

Sergeev, D.E., Renfrew, I.A., Spengler, T. and Dorling, S.R. (2017) Structure of a shear-line polar low. *Quarterly Journal of the Royal Meteorological Society*, 143(702), 12–26. https://doi.org/10.1002/qj.2911.

Shinoda, Y., Kawamura, R., Kawano, T. and Shimizu, H. (2021) Dynamical role of the Changbai Mountains and the Korean Peninsula in the wintertime quasi-stationary convergence zone over the Sea of Japan. *International Journal of Climatology*, 41(S1), E602–E615. https://doi.org/10.1002/joc.6713.

Spengler, T., Cloud, C. and Heinemann, G. (2017) Polar Low Workshop summary. *Bulletin of the American Meteorological Society*, 98(6), ES139–ES142. https://doi.org/10.1175/BAMS-D-16-0207.1.

Spensberger, C. and Spengler, T. (2021) Sensitivity of air–sea heat exchange in cold-air outbreaks to model resolution and sea-ice distribution. *Journal of Geophysical Research: Atmospheres*, 126(5), e2020JD033610. https://doi.org/10.1029/2020JD033610.

Steenburgh, W.J. and Campbell, L.S. (2017) The OWLeS IOP2b lake-effect snowstorm: Shoreline geometry and the mesoscale forcing of precipitation. *Monthly Weather Review*, 145(7), 2421–2436. https://doi.org/10.1175/mwr-d-16-0460.1.

Steenburgh, W.J. and Nakai, S. (2020) Perspectives on sea- and lake-effect precipitation from Japan's "gosetsu chitai". *Bulletin of the American Meteorological Society*, 101(1), E58–E72. https://doi.org/10.1175/BAMS-D-18-0335.1.

Stoll, P.J., Spengler, T., Terpstra, A. and Graversen, R.G. (2021) Polar lows—Moist-baroclinic cyclones developing in four different vertical wind shear environments. *Weather and Climate Dynamics*, 2, 19–36. https://doi.org/10.5194/wcd-2-19-2021.

Terpstra, A., Michel, C. and Spengler, T. (2016) Forward and reverse shear environments during polar low genesis over the northeast Atlantic. *Monthly Weather Review*, 144, 1341–1354. https://doi.org/10.1175/MWR-D-15-0314.1.

Terpstra, A., Renfrew, I.A. and Sergeev, D.E. (2021) Characteristics of cold-air outbreak events and associated polar mesoscale cyclogenesis over the North Atlantic region. *Journal of Climate*, 34, 4567–4584. https://doi.org/10.1175/JCLI-D-20-0595.1.

Terpstra, A. and Watanabe, S. (2020). Polar lows, *Oxford Research Encyclopedia of Climate Science*, https://doi.org/10.1093/acrefore/9780190228620.013.775.

Watanabe, S.I. and Niino, H. (2014) Genesis and development mechanisms of a polar mesocyclone over the Japan Sea. *Journal of the Atmospheric Sciences*, 142(6), 2248–2270. https://doi.org/10.1175/MWR-D-13-00226.1.

Watanabe, S.I., Niino, H. and Yanase, W. (2016) Climatology of polar mesocyclones over the Sea of Japan using a new objective tracking method. *Monthly Weather Review*, 144(7), 2503–2515. https://doi.org/10.1175/MWR-D-15-0349.1.

Watanabe, S.I., Niino, H. and Yanase, W. (2018) Composite analysis of polar mesocyclones over the western part of the Sea of Japan. *Monthly Weather Review*, 146(4), 985–1004. https://doi.org/10.1175/mwr-d-17-0107.1.

West, T.K. and Steenburgh, W.J. (2022) Formation, thermodynamic structure, and airflow of a Japan Sea polar airmass convergence zone. *Monthly Weather Review*, 150(1), 157–174. https://doi.org/10.1175/MWR-D-21-0095.1.

Yanase, W., Niino, H., Watanabe, S.I., Hodges, K., Zahn, M., Spengler, T. and Gurvich, I. (2016) Climatology of polar lows over the Sea of Japan using the JRA-55 reanalysis. *Journal of Climate*, 29(2), 419–437. https://doi.org/10.1175/JCLI-D-15-0291.1.

How to cite this article: Watanabe, S.I., Niino, H. & Spengler, T. (2022) Formation of maritime convergence zones within cold air outbreaks due to the shape of the coastline or sea ice edge. *Quarterly Journal of the Royal Meteorological Society*, 148(746), 2546–2562. Available from: https://doi.org/10.1002/qj.4324

APPENDIX

We considered an f-plane at 40°N for the control experiment, which is the typical latitude for CAOs in the Sea of Japan. However, with CAOs generally occurring at higher latitudes, such as the Nordic Seas, Labrador Sea and Southern Ocean around Antarctica, we examine the sensitivity of our results by changing the Coriolis parameter to an f-plane at 60°N, where we performed both a dry and moist experiment.

In the dry experiment, the results are similar to the control experiment (Figure A1a), which is consistent with the prediction from the analytic model. Although the Coriolis parameter at 60°N is 1.34 times larger than that at 40°N, it is still small compared with the friction coefficient. Therefore, the results of the numerical simulation are only negligibly affected by the Coriolis parameter. In the moist experiment, the southward deflection of the convergence zone is slightly larger than in the control experiment (Figure A1b), as the southward deflection is associated with the strength of the frontogenetic overturning connected to the Sawyer–Eliassen equation, which is proportional to the Coriolis parameter. Note that a mesoscale cyclone started to develop on the convergence zone at around $x = 2{,}300$ km and $y = 800$ km. The formation of the convergence zone itself, however, is not significantly affected by the Coriolis parameter.

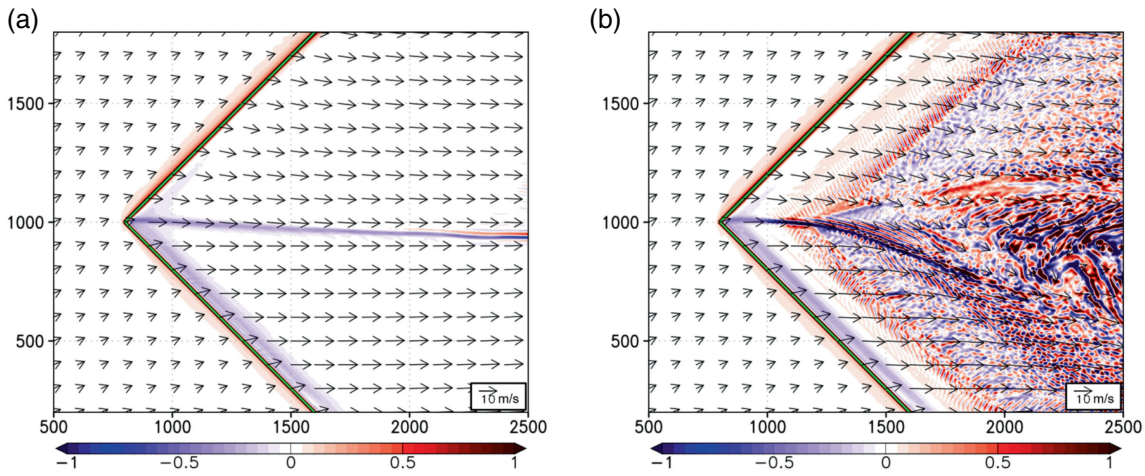

FIGURE A1 Same as Figures 3a and 6a but for the experiment with the Coriolis parameter at 60°N: (a) dry experiment; (b) moist experiment